Materials Science and Engineering A 498 (2008) 335–340

Contents lists available at ScienceDirect

Materials Science and Engineering A

journal homepage: www.elsevier.com/locate/msea

# Microstructural changes induced by thermal treatment in $Cu_{47}Ti_{33}Zr_{11}Ni_8Si_1$ metallic glass

J. Bednarcik[a], S. Venkataraman[b,*], O. Khvostikova[b], H. Franz[a], D.J. Sordelet[c], J. Eckert[b,d]

[a] HASYLAB am DESY, Notkestrasse 85, D-22603 Hamburg, Germany
[b] IFW Dresden, Institut für Komplexe Materialien, Helmholtzstraße 20, D-01069 Dresden, Germany
[c] Materials and Engineering Physics Program, Ames Laboratory (USDOE), Iowa State University, Ames, Iowa 50011, USA
[d] T U Dresden, Institut für Werkstoffwissenschaft, D-01062 Dresden, Germany

ARTICLE INFO

*Article history:*
Received 26 March 2008
Received in revised form 5 August 2008
Accepted 8 August 2008

*Keywords:*
Metallic glass
Synchrotron light
Thermal treatment
DSC
XRD

ABSTRACT

The influence of thermal treatment on structural changes in the $Cu_{47}Ti_{33}Zr_{11}Ni_8Si_1$ metallic glass has been monitored using X-ray diffraction (XRD) and differential scanning calorimetry (DSC). Additionally, the short-range order structure has been investigated by XRD using synchrotron radiation. The changes observed in the calorimetric behaviour cannot be quantified using conventional XRD. Small changes are, however, visible in the total structure factor $S(Q)$ primarily in terms of amplitude of the oscillations, which tend to increase with increasing thermal treatment temperature. Real-space analysis of the pair distribution function suggests that the first coordination shell consists of three peaks, which can be modelled using Gaussian distributions. Furthermore, the synchrotron data also reveal changes in the local structure that occur during structural relaxation and early formation of nanocrystals at temperatures close to the experimentally determined crystallization temperature.



## 1. Introduction

Bulk metallic glasses, as structural materials, have attracted much attention for their scientific purposes and technological applications due to their properties such as high strength as well as large elastic limit [1]. Structurally, metallic glasses can be classified as a disordered material [2]. Understanding the atomistic structure of metallic glasses has been a long standing issue that remains crucial for determining the relationships between structure and properties [1]. Typically, the structure of metallic glasses is studied using conventional X-ray diffraction (XRD) and transmission electron microscopy (TEM) [3]. However, conventional XRD, done either in reflection or transmission mode, has its limitations. Many reports have indicated that it fails to distinguish a true amorphous structure from a fine nanocrystalline structure, especially if the grain size is smaller than 10 nm [3–5]. Additionally, the very fact that laboratory XRD has a relatively larger wavelength means a limited range in reciprocal space. A direct observation technique such as TEM, on the other hand, can give information about the intrinsic microstructure [6]. However, TEM requires extensive preparation to produce a sample thin enough to be electron transparent. This is often a time consuming process. Samples also can undergo changes in the structure during the preparation process [7–9]. Moreover, the investigated volume is relatively small, raising the possibility that the region analyzed may not be characteristic of the whole sample. On the other hand, high-energy X-rays as provided by synchrotron radiation sources have the advantage of high penetration into most materials [10]. Hard X-rays are used because a high resolution in real-space, as desired for disordered materials, can be achieved and the required data corrections are small, particularly for absorption [10]. A range of wavelengths over a wide energy range can be used, which are typically around an order of magnitude lower than for conventional XRD [11]. The data acquisition time is extremely rapid in comparison with conventional XRD. Additionally, the signal-to-noise ratio is low. Synchrotron radiation operated in the transmission mode could help in identifying fine crystalline features, of the length scale of the order of 10 nm which are easily to be missed by conventional XRD [11]. Because of this, synchrotron radiation has been widely used to study the structure of metallic glasses [12–20].

The $Cu_{47}Ti_{33}Zr_{11}Ni_8Si_1$ metallic glass composition is fairly well studied. This composition is an excellent glass former with the ability to be cast in bulk form [21–23]. Previous studies on the calorimetric traces of $Cu_{47}Ti_{33}Zr_{11}Ni_8Si$ gas-atomized powder have indicated that a broad exothermic event precedes the appearance of the glass transition and the supercooled liquid region followed by subsequent crystallization [24]. The broad exotherm has been

* Corresponding author. Tel.: +49 351 4659747; fax: +49 351 4659452.
*E-mail address:* s.venkataraman@ifw-dresden.de (S. Venkataraman).

0921-5093/$ – see front matter © 2008 Elsevier B.V. All rights reserved.
doi:10.1016/j.msea.2008.08.016

explained in terms of structural relaxation as well as nanocrystallization [24]. In terms of the free volume theory, relaxation has been explained as to stem from topological short-range ordering (TSRO) as well as chemical short-range ordering (CSRO) [25]. TSRO is related to annihilation of excess free volume which gets quenched-in during the rapid cooling of the liquid [26]. CSRO, on the other hand, is commonly observed in multi-component glasses and is ascribed to redistribution of the constituent atoms [27]. Both TSRO and CSRO can cause microstructural changes. Hence, it is interesting to study these changes since the properties of materials are usually determined by their microstructure, namely, the nature, perfection, and spatial distribution of their component phases. In this work, synchrotron radiation studies have been carried out on the $Cu_{47}Ti_{33}Zr_{11}Ni_8Si_1$ metallic glass powders treated at different temperatures. It will be shown that fine-scale alterations which occur in the microstructure can be well-studied using high-energy synchrotron radiation.

## 2. Experimental procedure

Spherical powders of the $Cu_{47}Ti_{33}Zr_{11}Ni_8Si_1$ alloy were prepared by gas-atomization. The parameters employed for synthesis have been reported elsewhere [24]. Thermal treatments of the powder samples as well as calorimetric studies were done using a PerkinElmer DSC 7 differential scanning calorimeter (DSC) under high purity flowing Ar. The calorimeter was calibrated for temperature and energy with high purity indium and zinc standards. Isochronal DSC measurements were done at a heating rate of 20 K/min. For all the DSC runs, two successive runs were recorded with the second run serving as a baseline. This study deals with four different $Cu_{47}Ti_{33}Zr_{11}Ni_8Si_1$ powder samples. The individual samples and their thermal history were: Sample A: the gas atomized $Cu_{47}Ti_{33}Zr_{11}Ni_8Si_1$ powder in the as-prepared state. Sample B: $Cu_{47}Ti_{33}Zr_{11}Ni_8Si_1$ powder thermally treated up to 701 K. The thermal treatment involved constant-rate heating the powder up to 701 K at a heating rate of 40 K/min followed by cooling down to room temperature at 100 K/min. Sample C: $Cu_{47}Ti_{33}Zr_{11}Ni_8Si_1$ powder treated up to 723 K. For this type of sample, a similar DSC scheme as for sample B has been employed, except that the powder was heated up to 723 K. Sample D: $Cu_{47}Ti_{33}Zr_{11}Ni_8Si_1$ powder thermally treated up to 743 K, i.e. a similar DSC procedure has been done as for samples B and C but a final temperature of 743 K was used in this case. The intention of choosing these treatment temperatures was to study microstructural alterations, if any, which are possible in the glass transition region, using conventional XRD as well as synchrotron light and to compare the results.

Conventional XRD studies in transmission mode were carried out using a STOE diffractometer (molybdenum target, wavelength, $\lambda = 0.70932$ Å, operated at 50 kV, 30 mA). High-energy X-ray diffraction (XRD) measurements were performed at HASYLAB at DESY (Hamburg, Germany) on the wiggler beamline BW5 [28] at the DORIS III storage ring using monochromatic synchrotron radiation of 103.8 keV ($\lambda = 0.119441$ Å). The diffraction experiments were carried out in Debye–Scherrer geometry. Quartz capillaries with a diameter of 2 mm and 20 μm wall thickness were filled with powder samples. The samples measured at room temperature were illuminated for 20 s by a well-collimated incident beam with a cross-section of 1 mm × 1 mm. XRD patterns were collected using a MAR345 imaging plate detector mounted orthogonal to the X-ray beam. In order to cover the high-$Q$ range ($Q = 4\pi \sin(\theta)/\lambda$) up to 19 $Å^{-1}$ the XRD patterns were recorded in asymmetric mode (the imaging plate detector was shifted 7 cm relative to the beam path), and the distance between 2D detector and sample was adjusted to 60 cm. A $LaB_6$ standard was used to calibrate the sample-to-detector distance and the tilt of the imaging plate relative to the beam path. About five independent scans for each sample were averaged to attain optimum counting statistics. The background intensity was subtracted directly from the 2D XRD pattern, and the result was integrated to the $Q$-space using the software package FIT2D [29]. The integrated data were corrected for polarization, sample absorption, fluorescence contribution, and inelastic scattering using the PDFgetX2 software [30]. The total structural factor, $S(Q)$, is obtained from the normalized elastically scattered intensity using standard procedures described in [31]:

$$S(Q) = 1 + \frac{I_e(Q) - \left[\sum_{i=1}^{n} c_i f_i^2(Q)\right]}{\left[\sum_{i=1}^{n} c_i f_i(Q)\right]^2}, \quad (1)$$

where $c_i$ and $f_i(Q)$ are the atomic concentration and the scattering factor of the atomic species of type $i$ (i = Cu, Ti, Zr, Ni, Si), respectively. The total structure factor can be further written in the form

$$S(Q) = \sum_{i,j}^{n} w_{ij}(Q) S_{ij}(Q), \quad (2)$$

where $S_{ij}(Q)$ represents the partial structure factor and $w_{ij}$ is the weight of the $i$–$j$ pair, calculated in the following manner:

$$w_{ij} = \begin{cases} \dfrac{2c_i c_j f(Q) f_j(Q)}{\left[\sum_{k=1}^{n} c_k f_k(Q)\right]^2} & i \neq j \\ \dfrac{c_i^2 f_i^2(Q)}{\left[\sum_{k=1}^{n} c_k f_k(Q)\right]^2} & i = j \end{cases}. \quad (3)$$

The reduced pair distribution function, $G(r)$, can be obtained through a sine Fourier transform:

$$G(r) = 4\pi r[\rho(r) - \rho_0] = \frac{2}{\pi} \int_0^{Q_{max}} Q(S(Q) - 1)\, \sin(rQ) \mathrm{d}Q, \quad (4)$$

where $\rho(r)$ and $\rho_0$ are the *local* and *average* atomic number densities, respectively, and $r$ is the radial distance. From $G(r)$ the pair distribution function, $g(r)$, and radial distribution function, RDF($r$), can be calculated by

$$g(r) = \frac{\rho(r)}{\rho_0} = \frac{G(r)}{4\pi\rho_0 r} + 1, \quad (5)$$

$$\mathrm{RDF}(r) = 4\pi r^2 \rho(r) = 4\pi\rho_0 r^2 + rG(r). \quad (6)$$

The average coordination number, $N$, around any given atom in a spherical shell between radius $r_1$ and $r_2$ can be calculated as

$$N = \int_{r_1}^{r_2} \mathrm{RDF}(r) \mathrm{d}r. \quad (7)$$

## 3. Results and discussion

Fig. 1 shows the constant heating rate traces of the $Cu_{47}Ti_{33}Zr_{11}Ni_8Si_1$ powders. In the low temperature region (400–700 K), a broad exotherm is visible in case of the as-atomized powder. This exothermic event starts at about 420 K and has a minimum at about 560 K. The onset value of the glass transition temperature ($T_g$) for the as-atomized state is 690 K for a heating rate of 20 K/min and the onset value of the crystallization temperature ($T_x$) is 746 K. The extension of the supercooled liquid region ($\Delta T$), defined as the difference between $T_x$ and $T_g$ is 56 K. With increase in treatment temperatures, as seen in the case of samples B, C and D, there appears to be only a single endothermic event prior to the main crystallization event. The low-temperature exothermic event disappears. The $T_g$ values as well as the $T_x$ values are listed in Table 1. It can be seen that thermal treatment causes considerable changes in the value of $T_g$ while the changes in $T_x$ are not drastic.

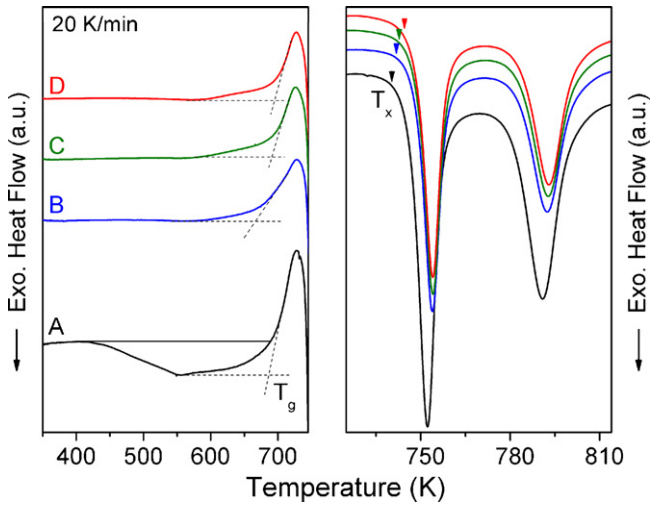


**Fig. 1.** Constant heating rate DSC traces of gas-atomized (A) and thermally treated (B–D) $Cu_{47}Ti_{33}Zr_{11}Ni_8Si_1$ powders. The temperature of the glass transition, $T_g$, and crystallization, $T_x$, are depicted.

Fig. 2a shows the XRD patterns obtained using a conventional XRD diffractometer. In case of the as-atomized state, the XRD pattern displays broad diffuse maxima, characteristic of an amorphous material. The XRD patterns of the thermally treated powders look very similar and do not give any evidence for crystallinity. A comparison of the XRD patterns given in Fig. 2a and b clearly demonstrates that the use of synchrotron radiation has several advantages over conventional X-ray diffractometry. Nearly noise-free XRD patterns in case of using synchrotron are result of (i) a very high photon flux and (ii) the area detector covering a relatively large solid angle of diffracted photons. Furthermore, the use of hard X-rays allows to perform diffraction experiments in transmission mode, which can help to suppress absorption when the sample thickness is appropriately selected. Simultaneously, it also allows an acquisition of data up to high momentum transfer vectors $Q$, which is a prerequisite for determination of the structure factor $S(Q)$ out to long reciprocal lengths, but more so for subsequently calculating the real-space pair distribution function $g(r)$. As can be seen from Fig. 2b, the as-atomized and annealed samples exhibit diffuse scattering patterns typical for metallic glasses with a maximum at $Q \sim 2.87\,\text{Å}^{-1}$ and pronounced oscillations visible up to $Q \sim 19\,\text{Å}^{-1}$.

After applying a set of corrections (polarization, sample absorption, fluorescence contribution and inelastic scattering) to the measured intensities, the total structure factors $S(Q)$ were determined (Fig. 3). From the first look they look rather similar. However, careful comparison indicates slight changes for the annealed samples. Namely, the amplitude of oscillations of $S(Q)$ is slightly higher compared to the as-atomized powder and tends to increase with increasing temperature. As can be seen from the inset in Fig. 3, annealing increases the intensity of the main peak. Difference curves (not shown here) confirm that annealing increases the

**Table 1**
Glass transition temperature, $T_g$, crystallization temperature, $T_x$, and extension of the supercooled liquid region ($\Delta T = T_x - T_g$) of gas-atomized (A) and thermally treated (B–D) $Cu_{47}Ti_{33}Zr_{11}Ni_8Si_1$ powder samples as obtained from DSC measurements

| Label | Condition | $T_g$ (±1 K) | $T_x$ (±1 K) | $\Delta T$ (K) |
|---|---|---|---|---|
| A | As-atomized | 690 | 746 | 56 |
| B | 701 K | 671 | 750 | 79 |
| C | 723 K | 689 | 748 | 59 |
| D | 743 K | 694 | 748 | 54 |

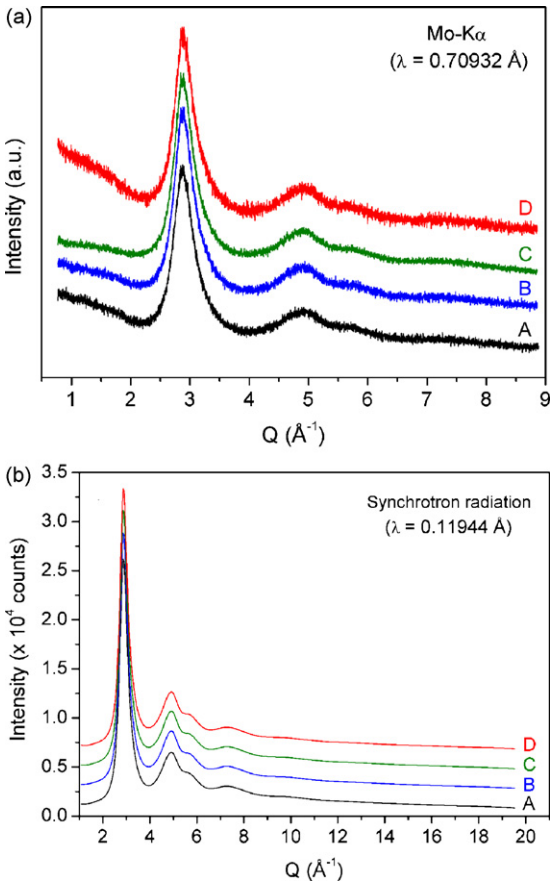


**Fig. 2.** Comparison of XRD patterns obtained (a) in transmission geometry using a conventional diffractometer equipped with Mo target and (b) in transmission geometry using a triple-crystal diffractometer at the HASYLAB wiggler beamline BW5 [28].

amplitude of the oscillations and visible changes in $S(Q)$ can be observed up to $10\,\text{Å}^{-1}$. Such changes in $S(Q)$ indicate microstructural changes in the amorphous material upon annealing.

In order to relate such changes in reciprocal space with changes real space one has to perform a Fourier transformation of the

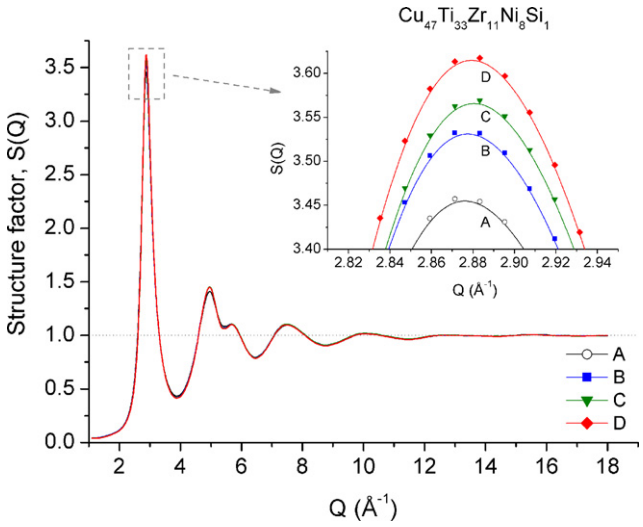


**Fig. 3.** The total structure factors of gas-atomized (A) and thermally treated (B–D) $Cu_{47}Ti_{33}Zr_{11}Ni_8Si_1$ powder. The inset shows a detailed view of the first diffuse peak for the as-prepared and thermally treated samples.

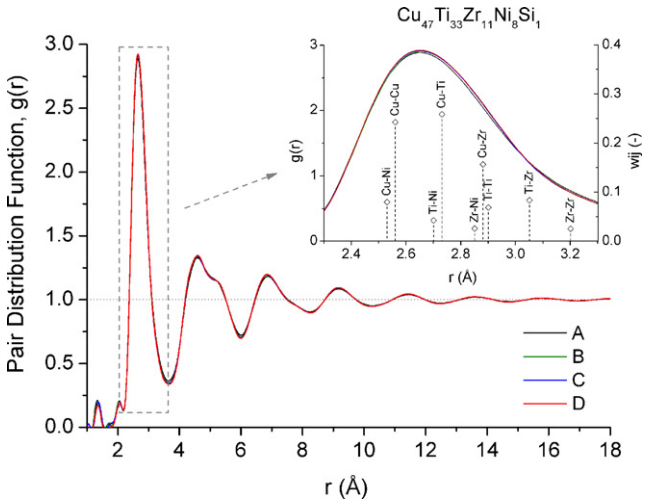


**Fig. 4.** Pair distribution functions $g(r)$ of gas-atomized (A) and thermally treated (B–D) $Cu_{47}Ti_{33}Zr_{11}Ni_8Si_1$ samples. The inset shows a detailed view of the first coordination shell together with the theoretical bond lengths (explicitly listed in Table 2).

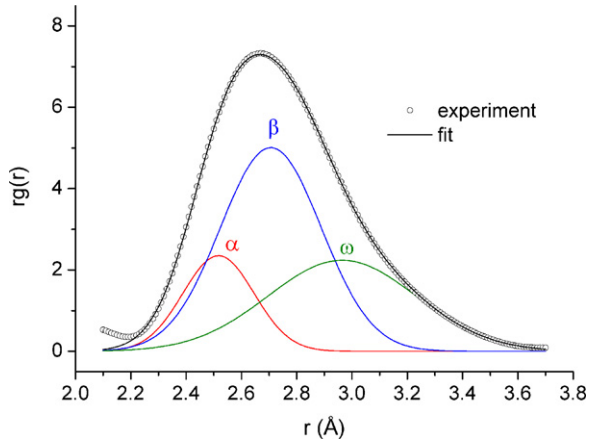


**Fig. 5.** Deconvolution of the first coordination shell into three Gaussians for an as atomized powder sample (A).

structure factor $S(Q)$, according to Eq. (4). Fig. 4 shows the pair distribution functions $g(r)$ calculated from the corresponding $S(Q)$'s by applying Eq. (5). The inset in Fig. 4 shows a detailed view of the first broad maximum in $g(r)$ together with the interatomic bond lengths (sum of atomic radii) and the corresponding weight factors $w_{ij}$ (denoted by open diamonds), explicitly listed in Table 2. For the $Cu_{47}Ti_{33}Zr_{11}Ni_8Si_1$ glass, there are 15 possible nearest-neighbour partials with corresponding X-ray weights $w_{ij}$. Due to similar size and electronic properties of Cu and Ni and low concentration of weak scatterer such as Si, one can treat given alloy as a pseudo-ternary system (Cu,Ni)–Ti–Zr. Such simplification reduces the number of nearest-neighbour partials to six ((Cu,Ni)–(Cu,Ni), Ti–(Cu,Ni), Zr–(Cu,Ni), Ti–Ti, Ti–Zr and Zr–Zr). From the type and concentration of constituent elements in the alloy it is clear that the dominant atomic pairs which determine the shape of the $g(r)$'s are Cu–Ti, Cu–Cu, Cu–Zr, Cu–Ni, Ti–Zr, and Ti–Ti (ordered by their weighting factors $w_{ij}$). A similar approach for analyzing a multicomponent Zr-based metallic glass has been reported recently [20]. It should be noted here that the theoretical bond lengths obtained as a sum of atomic radii are overestimated in case of atomic pairs exhibiting a negative heat of mixing. For example, the enthalpy of mixing for Cu–Zr (−23 kJ/mol [32]) indicates strong attractive interactions between these pairs. Thus, it is energetically favourable for part of the Cu atoms to be surrounded by Zr. This explains why the interatomic distance of Cu–Zr pairs is usually found to be significantly smaller than the corresponding sum of atomic radii [33]. Previous measurements on $Cu_{50}Zr_{50}$ [34] and $Cu_{46}Zr_{54}$ [35] glasses have proved that the typical interatomic bond length of the Cu–Zr pair is 2.75 Å, which is 0.13 Å smaller as predicted from the sum of the metallic radii (see Table 2). The same effect can be expected for Zr–Ni pair which also exhibits a negative enthalpy of mixing (−49 kJ/mol [32]). It should be noted here that the decomposition of the first coordination shell (the first peak appearing in the pair distribution function) into six partials from only one independent measurement (in our case X-ray diffraction) is ambiguous. Despite this fact we modelled the first coordination shell using three Gaussians in order to describe the changes in the microstructure of amorphous alloy upon thermal treatment more quantitatively. Based on atomic sizes, X-ray weights and the above-mentioned facts we divided the atomic pairs into three groups (Cu–Cu, Cu–Ni), (Cu–Ti, Cu–Zr, Ti–Ni) and (Ti–Zr, Ti–Ti, Zr–Zr, Zr–Ni) noted as α, β and ω, respectively. It was previously shown that for isotropic systems such as amorphous alloys, the atomic pair distributions in $rg(r)$ follow Gaussian profiles [36]. Therefore, the first coordination shell was modelled with three partials α, β and ω, all having Gaussian profile. Fig. 5 shows the result of the best fit to $rg(r)$ for the as-atomized powder (sample A) after subtracting background due to overlapping contributions from the second shells. The same procedure was repeated for the heat-treated powders B, C and D. The results of the quantitative analysis are presented in Table 3. With increasing temperature all peaks shift slightly towards higher $r$-values. On the other hand, the relative areas of α and β tend to grow with increasing temperature at the expense of ω, resulting in a sharpening of the first shell. The third Gaussian ω is relatively broad compared to α and β since it represents more pairs having different interatomic separations. The coordination number, $N$, calculated according to Eq. (6) from the first coordination shell

**Table 2**
Fifteen possible nearest-neighbour atomic pairs in the $Cu_{47}Ti_{33}Zr_{11}Ni_8Si_1$ alloy and their theoretical bond lengths [$r_{ij}$, sum of atomic radii (1.28, 1.45, 1.6, 1.25 and 1.17 Å for Cu, Ti, Zr, Ni and Si, respectively)] and weighting factors $w_{ij}$ calculated at $Q = 0$ Å$^{-1}$ according to Eq. (3)

| Atomic pair | $r_{ij}$ (Å) | $w_{ij}$ |
|---|---|---|
| Cu–Cu | 2.56 | 0.2426 |
| Cu–Ti | 2.73 | 0.2585 |
| Cu–Zr | 2.88 | 0.1566 |
| Cu–Ni | 2.53 | 0.0798 |
| Cu–Si | 2.45 | 0.0050 |
| Ti–Ti | 2.90 | 0.0689 |
| Ti–Zr | 3.05 | 0.0834 |
| Ti–Ni | 2.70 | 0.0425 |
| Ti–Si | 2.62 | 0.0027 |
| Zr–Zr | 3.20 | 0.0253 |
| Zr–Ni | 2.85 | 0.0257 |
| Zr–Si | 2.77 | 0.0016 |
| Ni–Ni | 2.50 | 0.0066 |
| Ni–Si | 2.42 | 0.0008 |
| Si–Si | 2.34 | 0.0000 |

**Table 3**
Best-fit peak position $r_{ij}$ (±0.01 Å) and relative peak area $S$ (±1%) of the three Gaussians α, β and ω obtained from deconvolution of the first coordination shell

| Gaussian | Peak position (±0.01 Å) | | | | Relative peak area (±1%) | | | |
|---|---|---|---|---|---|---|---|---|
| | A | B | C | D | A | B | C | D |
| α | 2.517 | 2.523 | 2.526 | 2.528 | 16.64 | 18.88 | 21.72 | 21.99 |
| β | 2.706 | 2.722 | 2.737 | 2.739 | 50.50 | 53.19 | 56.38 | 55.57 |
| ω | 2.964 | 2.993 | 3.045 | 3.044 | 32.86 | 27.93 | 21.90 | 22.44 |

(range 2.2–3.6 Å) of the radial distribution function RDF($r$) is equal to $13 \pm 0.2$ and does not change with thermal treatment within the experimental error.

The observed changes in the first coordination shell suggest changes in the short-range order of the gas-atomized powder upon heat treatment below the crystallization temperature. This is clearly seen from the difference between the pair distribution function (PDF) for samples A and B shown in Fig. 6 (top). The difference is negative at short as well as long distances. However, around the centre of the first PDF peak it is positive. This indicates that treatment as done for sample B leads to elimination of short and long interatomic distances while the density of average distances is increased. However for treatments as done for samples C and D, Fig. 6 (center and bottom plots), the changes in the main PDF peak are small. Similar observations have been also made based on neutron diffraction studies in case of Zr-based metallic glass annealed below the glass transition temperature [37]. Furthermore, a detailed analysis of the two-dimensional diffraction images shows that annealing at temperatures 723 K (sample C) and 743 K (samples D) already induces the formation of nanocrystals. As an example, Fig. 7 shows a zoomed part of a two-dimensional diffraction pattern of sample C, revealing the presence of distinct spots originating from Bragg diffraction of crystals. As five independent scans have been performed for each sample, it can be said that the observation that the spots appear at different distances from the origin indicates different diffraction planes while the change of their azimuth coordinate is due to a slight change of the sample position relative to the beam when moving the sample in and out of the beam for background measurement. The spots were observed at positions corresponding to Debye–Scherrer rings belonging to diffraction planes having $d$-spacing of 1.094, 1.282 and 2.027 Å. It should be noted here that these spots are of low intensity and after radial integration of the whole patterns they are averaged out. Hence, the integrated XRD patterns presented in Fig. 2b do not show any hint of corresponding Bragg peaks. The glass transition temperature as measured at 20 K/min for sample A is determined to be 690 K (Table 1). $T_x$ is found to be 746 K. Hence, the thermal treatments, that have been carried out for samples B, C and D correspond to treatments in the supercooled liquid region. It is well known that the supercooled liquid region is characterized by viscosity changes of 2–3 orders of magnitude [38], i.e. the viscosity of the supercooled liquid decreases with increasing temperature. Since viscosity and diffusivity are inversely related [39], the diffusion increases in the supercooled liquid region. Diffusion of atoms makes it feasible for clusters which may temporarily adopt the structure of the crystalline solid to be converted to stable nuclei by transfer of atoms across the interface. Hence, there is the possibility of short-range ordering/crystallization during thermal treatment. The changes observed in Fig. 3 and the quantitative changes observed in Table 3 are a manifestation of the microstructural changes caused due to the thermal treatment. Previous microstructural studies using TEM have found that thermal treatment in the supercooled liquid region also leads to formation of 4–6 nm sized nanocrystals in a predominantly amorphous matrix [40]. However, conventional XRD fails to detect the presence of these nanocrystals [40]. Thus, synchrotron radiation measurements as shown here are useful in this aspect and can give qualitative as well as quantitative information about the microstructural changes taking place in the material.

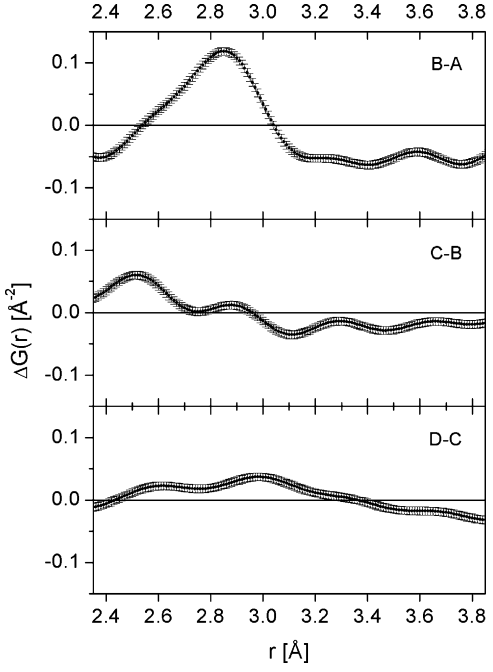


**Fig. 6.** Difference in pair distribution function of $Cu_{47}Ti_{33}Zr_{11}Ni_8Si_1$ powders: (top) B-A; (center) C-B; (bottom) D-C.

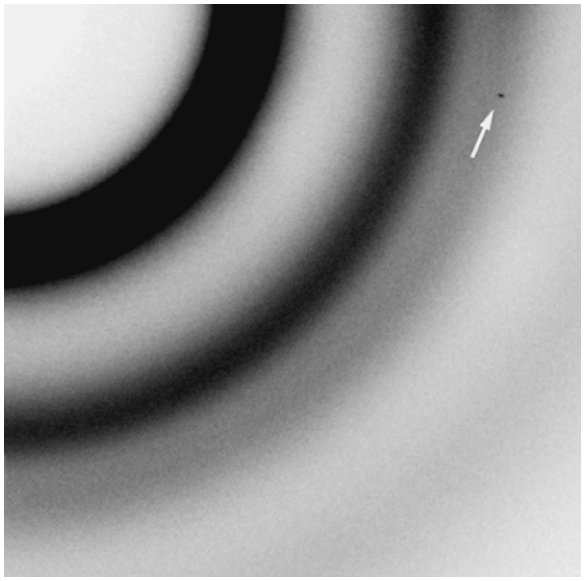

**Fig. 7.** Detailed view of a two-dimensional diffraction pattern of sample C showing a distinct spot (marked by the arrow) originating from Bragg diffraction of a crystalline component.

## 4. Conclusions

$Cu_{47}Ti_{33}Zr_{11}Ni_8Si_1$ metallic glass powders synthesized by gas-atomization and subsequently thermally treated have been characterized using conventional XRD, DSC and synchrotron light. Calorimetric investigations reveal that the as-atomized $Cu_{47}Ti_{33}Zr_{11}Ni_8Si_1$ alloy exhibits a broad exothermic event which is due to structural relaxation as well as nanocrystallization. Thermal treatment, as evinced in the calorimetric trace leads to disappearance of this broad exotherm. Conventional XRD fails to detect this change. Conversely, synchrotron data show changes in the local structure that occur due to either structural relaxation as well as formation of nanocrystals. The differences observed are in the total structure factor. The differences in the first coordination shell upon thermal treatment can be successfully modelled using Gaussian profiles.

## Acknowledgements

Funding for this work was provided by the German Research Foundation under grant no. Ec 111/10. The synthesis efforts by DJS were supported by the U.S. Department of Energy, Basic Energy Sciences, through Iowa State University under Contract No. W-7405-ENG-82.

## References

[1] A.L. Greer, E. Ma, MRS Bull. 32 (2007) 611–615.
[2] A.R. Yavari, Nat. Mater. 6 (2007) 181–182.
[3] W.H. Wang, C. Dong, C.H. Shek, Mater. Sci. Eng. R 44 (2004) 45–89.
[4] J.Z. Jiang, H. Kato, T. Ohsuna, J. Saida, A. Inoue, K. Saksl, H. Franz, K. Stahl, Appl. Phys. Lett. 83 (2003) 3299–3301.
[5] L.Q. Xing, T.C. Hufnagel, J. Eckert, W. Löser, L. Schultz, Appl. Phys. Lett. 77 (2000) 1970–1972.
[6] G. Thomas, M.J. Goringe, Transmission Electron Microscopy of Materials, first edition, John Wiley & Sons, New York, 1979.
[7] D.J. Barber, Ultramicroscopy 52 (1993) 101–125.
[8] B.B. Sun, Y.B. Wang, J. Wen, H. Yang, M.L. Sui, J.Q. Wang, E. Ma, Scripta Mater. 53 (2005) 805–809.
[9] H.J. Chang, E.S. Park, Y.C. Kim, D.H. Kim, Mater. Sci. Eng. A 406 (2005) 119–124.
[10] H.F. Poulsen, J. Neuefeind, H.-B. Neumann, J.R. Schneider, M.D. Zeidler, J. Non-Cryst. Solids 188 (1995) 63–74.
[11] K.D. Liss, A. Bartels, A. Schreyer, H. Clemens, Textures Microstruct. 35 (2003) 219–252.
[12] D.J. Sordelet, M.J. Kramer, M.F. Besser, E. Rozhkova, J. Non-Cryst. Solids 290 (2001) 163–172.
[13] N. Mattern, U. Kühn, H. Hermann, H. Ehrenberg, J. Neuefeind, J. Eckert, Acta Mater. 50 (2002) 305–314.
[14] J.Z. Jiang, K. Saksl, J. Saida, A. Inoue, H. Franz, K. Messel, C. Lathe, Appl. Phys. Lett. 80 (2002) 781–783.
[15] J.Z. Jiang, B. Yang, K. Saksl, H. Franz, N. Pryds, J. Mater. Res. 18 (2003) 895–898.
[16] L. Yang, Y. Chao, K. Saksl, H. Franz, L.L. Sun, W.K. Wang, N.P. Jiang, X.J. Wu, J.Z. Jiang, Appl. Phys. Lett. 84 (2004) 4998–5000.
[17] A.R. Yavari, A. Le Moulec, A. Inoue, N. Nishiyama, N. Lupu, E. Matsubara, W.J. Botta, G. Vaughan, M. Di Michiel, Å. Kvick, Acta Mater. 53 (2005) 1611–1619.
[18] N. Mattern, J. Non-Cryst. Solids 353 (2007) 1723–1731.
[19] H.W. Sheng, H.Z. Liu, Y.Q. Cheng, J. Wen, P.L. Lee, W.K. Luo, S.D. Shastri, E. Ma, Nat. Mater. 6 (2007) 192–197.
[20] M.J. Kramer, R.T. Ott, D.J. Sordelet, J. Mater. Res. 22 (2007) 382–388.
[21] H.C. Yim, R. Busch, W.L. Johnson, J. Appl. Phys. 83 (1998) 7993–7997.
[22] E.S. Park, H.K. Lim, W.T. Kim, D.H. Kim, J. Non-Cryst. Solids 298 (2002) 15–22.
[23] S. Venkataraman, M. Stoica, S. Scudino, C. Mickel, T. Gemming, U. Kunz, K.B. Kim, L. Schultz, J. Eckert, Scripta Mater. 54 (2006) 835–840.
[24] S. Venkataraman, S. Scudino, J. Eckert, T. Gemming, C. Mickel, L. Schutltz, D.J. Sordelet, J. Mater. Res. 21 (2006) 597–607.
[25] A. Vandenbeukel, J. Sietsma, Acta Metall. Mater. 38 (1990) 383–389.
[26] M.H. Cohen, D. Turnbull, J. Chem. Phys. 31 (1959) 1164–1169.
[27] T. Egami, Mater. Res. Bull. 13 (1978) 557–562.
[28] R. Bouchard, D. Hupfeld, T. Lippmann, J. Neuefeind, H.-B. Neumann, H.F. Poulsen, U. Rütt, T. Schimdt, J.R. Schneider, J. Süssenbach, M. von Zimmermann, J. Synchrotron Rad. 5 (1998) 90–101.
[29] A.P. Hammersley, S.O. Svensson, M. Hanfland, A.N. Fitch, D. Hausermann, High Press. Res. 14 (1996) 235–248.
[30] X. Qiu, J.W. Thompson, S.J.L. Billinge, J. Appl. Cryst. 37 (2004) 678.
[31] T. Egami, S.J.L. Billinge, Underneath the Bragg Peaks: Structural Analysis of Complex Materials, Pergamon Press, Oxford, 2003.
[32] F.R. de Boer, R. Boom, W.C.M. Mattens, A.R. Miedema, A.K. Nissen, Cohesion in Metals: Transition Metal Alloys, first edition, North Holland, Amsterdam, 1989.
[33] A. Sadoc, J.C. Lasjaunias, J. Phys. F: Met. Phys. 15 (1985) 1021–1031.
[34] H.S. Chen, Y. Waseda, Phys. Stat. Sol. A 51 (1979) 593–599.
[35] G. Duan, D.H. Xu, Q. Zhang, G.Y. Zhang, T. Cagin, W.L. Johnson, W.A. Goddard, Phys. Rev. B 71 (2005) 2242081–2242089.
[36] D.A. Dimitrov, H. Roder, A.R. Bishop, Phys. Rev. B 64 (2001) 0143031–0143038.
[37] D. Dmowski, C. Fan, M.L. Morrison, P.K. Liaw, T. Egami, Mater. Sci. Eng. A 471 (2007) 125–129.
[38] D. Turnbull, Sci. Am. 212 (1965) 38–46.
[39] J.F. Löffler, Intermetallics 11 (2003) 529–540.
[40] S. Venkataraman, H. Hermann, C. Mickel, L. Schultz, D.J. Sordelet, J. Eckert, Phys. Rev. B 75 (2007) 1042061–1042069.